New Journal of Physics
The open access journal at the forefront of physics

Deutsche Physikalische Gesellschaft DPG
IOP Institute of Physics

Published in partnership with: Deutsche Physikalische Gesellschaft and the Institute of Physics

OPEN ACCESS

RECEIVED
4 January 2022

REVISED
22 March 2022

ACCEPTED FOR PUBLICATION
29 March 2022

PUBLISHED
25 April 2022

PAPER

Toward ferromagnetic semimetal ground state with multiple Weyl nodes in van der Waals crystal $MnSb_4Te_7$

Jia-Yi Lin, Zhong-Jia Chen, Wen-Qiang Xie, Xiao-Bao Yang and Yu-Jun Zhao*

Department of Physics, South China University of Technology, Guangzhou 510640, People's Republic of China
* Author to whom any correspondence should be addressed.

E-mail: zhaoyj@scut.edu.cn

Keywords: first-principles calculations, magnetic phase transition, van der Waals materials

Abstract

The magnetic topological van der Waals materials family $MnBi_2Te_4/(Bi_2Te_3)_n$ have drawn markedly attention due to their novel multiple topological phases in different magnetic configurations. Recently, their close relative, the $MnSb_4Te_7$, was firstly synthesized in experiments (2021 *Phys. Rev. Lett.* **126** 246601). To further explore the emergent properties of $MnSb_4Te_7$, we have systematically investigated the magnetic and topological characters under compressive strain and charge doping using first-principles calculations. We predict that $MnSb_4Te_7$ transits from an interlayer antiferromagnetic ground state to a ferromagnetic semimetal ground state with multiple Weyl points when compressive strained along *c* axis above 8% or charge doping before 0.1 hole/formula concentration. Notable anomalous Hall conductivity is also predicted. Meanwhile, the magnetic easy axis can be reoriented from out-of-plane to in-plane orientation when strain or electron doping is applied. The underlying magnetic exchange mechanism is also analyzed from our calculation results. Our work thus provides a feasible way to realize applications of the highly tunable magnetic-topological nature and a comprehensive theoretical understanding of this magnetic topological material.

1. Introduction

As one of the most fantastic area of condensed matter physics, topological materials have roused a great deal of interest in the past two decades due to their unconventional physical properties [1–6]. A series of topological phase and topological materials, such as topological insulator, Dirac semimetal, Weyl semimetal, nodal line semimetal, axion insulator, topological Mott insulator, and high order topological insulator, were proposed theoretically and realized experimentally [7–16]. They exhibit plenty of robust physical phenomenons protected by symmetries, such as integer quantum Hall effect, quantum spin Hall effect and quantum anomalous Hall effect, and therefore become excellent platforms for future spintronics applications [17, 18].

The topological properties and unconventional surface or edge states of magnetic topological materials are always strongly coupled to the magnetic degrees of freedom [19]. Especially, the magnetic topological van der Waals crystal family, $MnX_2Te_4/(X_2Te_3)_n$ (X = Bi, Sb), has been intensively researched in past two years. The parent material, $MnBi_2Te_4$, was predicted and observed to be the first antiferromagnetic (AFM) topological insulator [20, 21]. It is an AFM axion insulator and an FM Weyl semimetal as well [22], which is much easier to manipulate the properties than the pioneering Weyl semimetal [23]. Subsequently, quantum anomalous Hall effect was observed in $MnBi_2Te_4$ experimentally [24, 25]. Similar phenomenons were also observed in $MnBi_4Te_7$ and $MnBi_8Te_{13}$ even under high temperature [26–29]. Meanwhile, topological superconductor phase and Majorana edge states were predicted in $MnBi_2Te_4$ and $MnBi_4Te_7$ [30, 31]. Since the strong coupling between the topological properties and the magnetic degrees of freedoms, this material family can also be the candidates for multiple topological materials. Robust topological axion insulator states also occurred in $MnBi_2Te_4$ [32, 33]. It is worth to note that their topological surface states are quite stable even in finite temperature [34, 35]. As for the $MnSb_2Te_4/(Sb_2Te_3)_n$ relatives, they remain much less

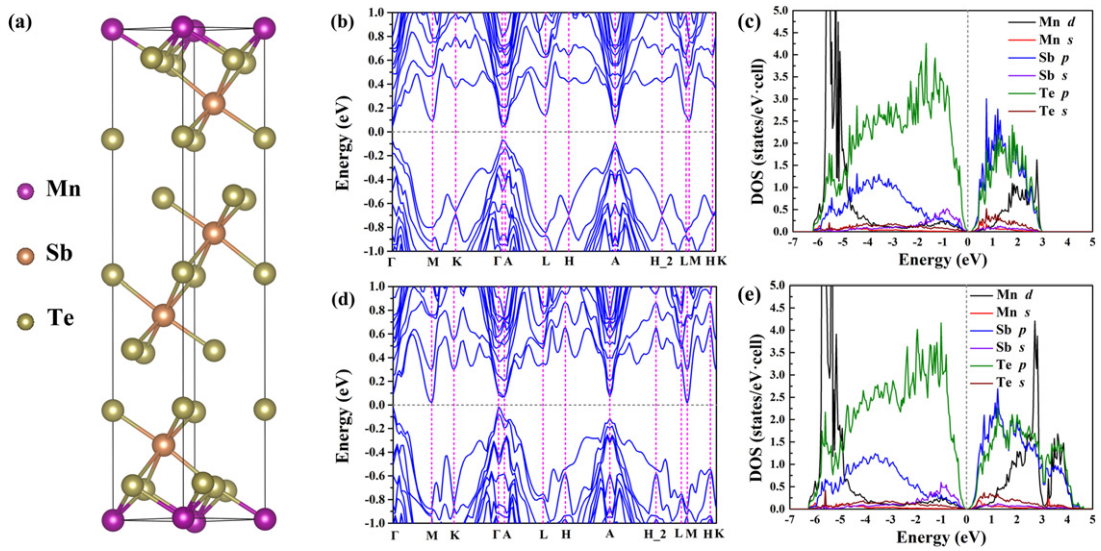

Figure 1. Structures and electronic properties of $MnSb_4Te_7$. (a) The crystal structure, (b) the interlayer AFM band structure, (c) the interlayer AFM PDOS, (d) the FM band structure, (e) the FM PDOS.

Table 1. The calculated and experimental lattice parameters of $MnSb_4Te_7$.

	Theo. value (Å)	Expt. value (Å)	Reference
a	4.2636	4.25	
b	4.2636	4.25	
c	23.6757	23.76	[38]

explored compared to $MnBi_2Te_4/(Bi_2Te_3)_n$. $MnSb_2Te_4$ is topologically trivial no matter in ferromagnetic (FM) or AFM configurations. Nevertheless, it can be driven into an FM Weyl semimetal state when compressive strain is applied [36]. Other relative compounds with $n > 1$ were predicted to be topologically non-trivial theoretically as well. However, most of them need to be confirmed in experiments [37].

Recently, $MnSb_4Te_7$ was firstly successfully prepared in experiments and confirmed to be a multiple magnetic topological van der Waals crystal by Huan *et al* [38]. Its ideal structure was predicted to be in interlayer AFM ground state with both topological insulator state and axion insulator state. The corresponding massless Dirac surface state is in the *S*-preserving surface and the gapped surface state is in the (0001) surface, where *S* is the time-reversal operation times the $\frac{1}{2}$ lattice translation along *c* axis [37]. In FM configuration, it is converted to an inversion-protected axion insulator [38]. When it is electron or hole doped, it behaves as a semimetal with multiple Weyl nodes appear in both conduction and valence bands [38]. Furthermore, the synthesized samples was slightly hole doped and behave like a Weyl semimetal, confirmed by the measured large anomalous Hall current. Generally speaking, the magnetic performance in van der Waals materials can be easily tuned by external conditions, such as strain, doping, defect, and charge, etc [39, 40]. Due to the strongly coupled magnetic-topological properties, the band topology could be manipulated at the same time in magnetic topological van der Waals materials. Such phenomenons extensively exist in $MnBi_2Te_4/(Bi_2Te_3)_n$ and $MnSb_2Te_4$ [41–57]. Additionally, ideal type-II Weyl semimetal states was firstly observed in the doped $Mn(Bi_{1-x}Sb_x)_2Te_4$ [58]. However, such tunable magnetic-topological performance in the newly synthesized $MnSb_4Te_7$ is remained to be explored and desired yet.

In this work, we systematically study the magnetic properties and band topology of $MnSb_4Te_7$ via first-principles calculations under compressive strain and charge doping conditions. We predict that $MnSb_4Te_7$ can be manipulated into FM ground states when strain or hole doping is applied. Furthermore, it could behave like a semimetal with multiple Weyl nodes existing in both conduction and valence bands. Large anomalous Hall conductivity (AHC) is also predicted. The magnetic easy axis can be reoriented from out-of-plane to in-plane orientation when compressive strained along *c* axis upon 10% or 0.2 electron/formula (f.u.) charge doped. It is worth to note that the magnetic anisotropic energy (MAE)

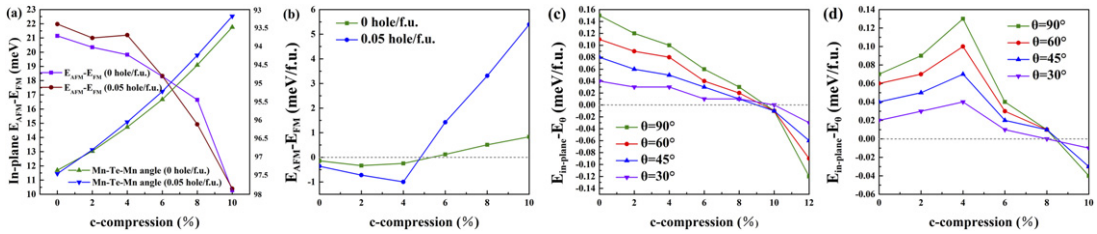

Figure 2. The AFM–FM transition and magnetic easy axis reorientation of $MnSb_4Te_7$ under *c*-compression. (a) The variance of intralayer magnetic exchange energy and Mn–Te–Mn bond angle as *c*-compressed, (b) the variance of interlayer magnetic exchange energy as *c*-compressed, (c) the variance of MAE as *c*-compressed, (d) the variance of MAE as *c*-compressed when charge doped 0.05 hole/f.u.

Table 2. The fractional coordinates of Weyl nodes in $MnSb_4Te_7$ found in 1 meV range near the Fermi level.

State	Coordinate
c-compression 8%	±(0.046 14, −0.001 44, 0.242 01)
Charge doped 0.05 hole/f.u.	±(0.136 89, −0.137 57, −0.169 97)
Charge doped 0.1 hole/f.u.	±(0.116 99, 0.015 60, −0.008 04)
Charge doped 0.05 electron/f.u.	±(0.031 88, −0.063 78, 0.360 00) ±(0.031 65, 0.030 68, 0.365 98) ±(0.030 90, 0.061 24, 0.360 04) ±(0.061 14, −0.031 10, −0.335 49) ±(0.062 43, −0.063 57, −0.340 45) ±(0.060 74, −0.030 77, −0.341 36)

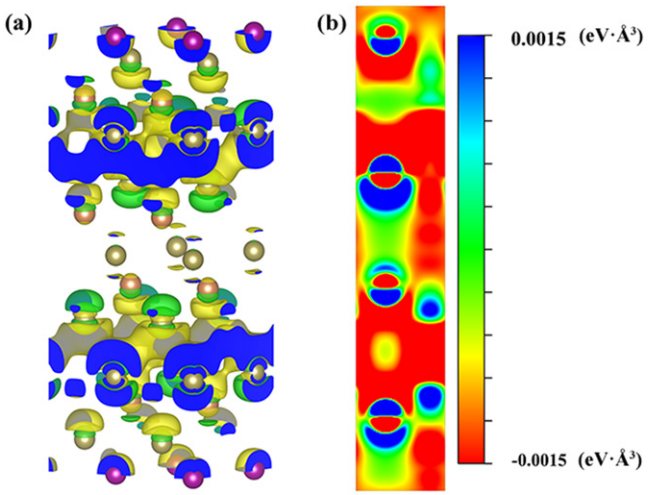

Figure 3. The deformation charge density of $MnSb_4Te_7$ between no charge doped and hole doped states. (a) The three dimension deformation charge density, (b) the deformation charge density of the (0, −1, 0) plane.

reaches a large value of 0.44 meV/f.u. when charge doped 0.3 electron/f.u. Based on our analysis, it is expected that the interlayer magnetic exchange is Ruderman–Kittel–Kasuya–Yosida (RKKY) exchange while the intralayer one is Mn 3*d*-Te 5*p*-Mn 3*d* super exchange as reported in earlier work [21, 38, 59].

2. Computational details

All our simulations are based on density functional theory combined with Hubbard *U* (DFT + *U*) method [60]. The projector-augmented wave (PAW) method is adopted [61]. The Vienna *ab initio* simulation package (VASP) is used all through our calculation [62–65]. Our computations are done within the meta-generalized gradient approximation (meta-GGA), using the strongly constrained and appropriately

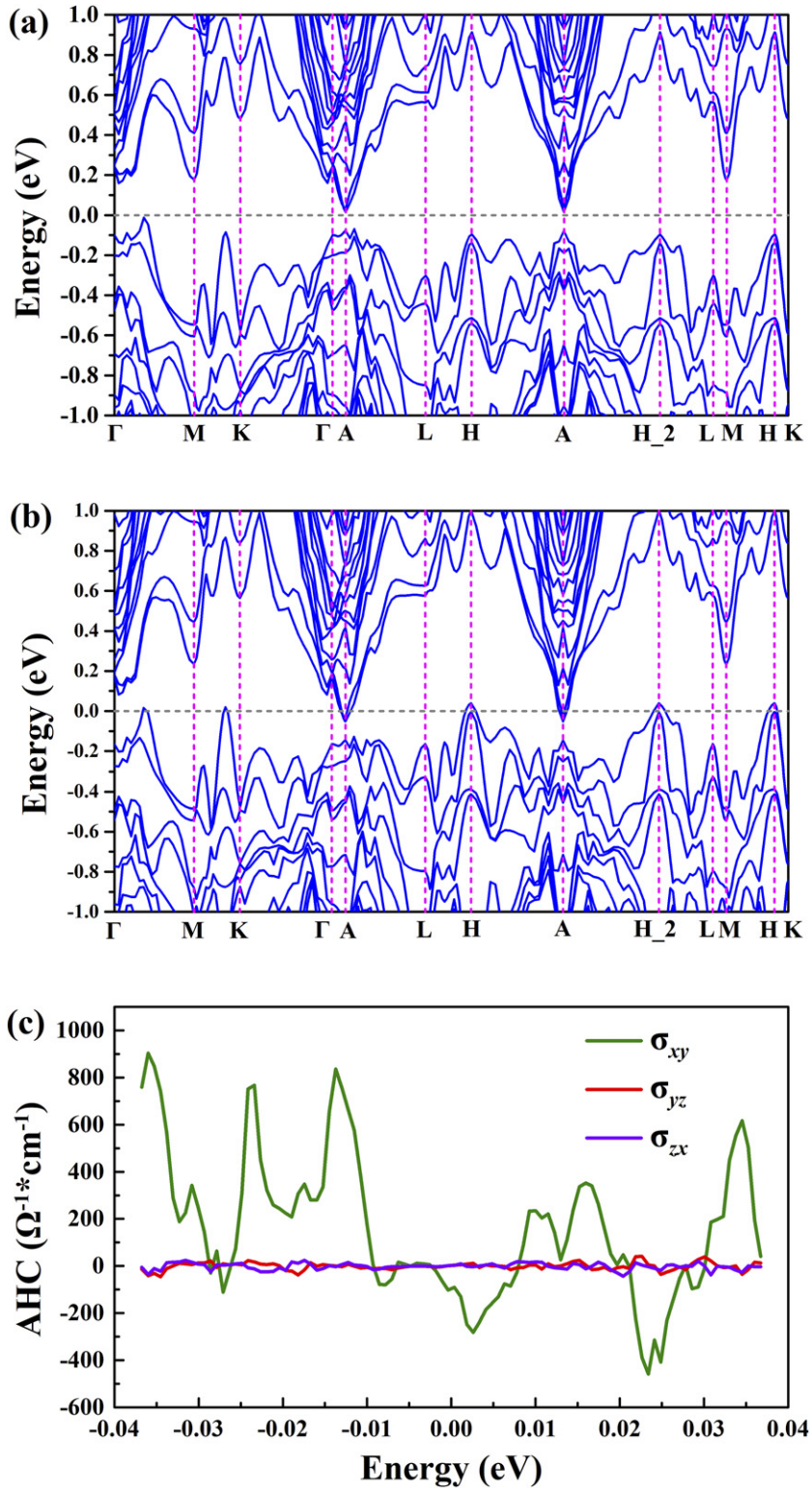

Figure 4. The insulator–metal transition and AHC of $MnSb_4Te_7$ under *c*-compression. (a) The band structure when *c* is compressed by 6%, (b) the band structure when *c* is compressed by 8%, (c) the AHC when *c* is compressed by 8%.

normed (SCAN) functional [66]. The SCAN functional is the first semilocal density functional that fulfills all known 17 constraints that an exact density functional must fulfill, which is believed to be more accurate than other semilocal density functionals but much more efficient than hybrid density functionals in series of tests [67]. To appropriately include the strong electron correlations of the Mn 3*d* orbitals, we adopt the on-site Coulomb interaction and exchange parameters of $U = 3.9$ eV and $J = 0.9$ eV, similar to the previous work [38]. We have also tested values of $U = 6.34$ eV and $J = 1$ eV to comfirm our conclusions are qualitatively stable against this range of U values. The energy cutoff for the plane wave basis set to expand

the Kohn–Sham wavefunction is set to 530 eV. All the coordinations of the atoms are fully relaxed until the residual forces on each atom are smaller than 0.001 eV Å^{-1}. The energy convergence criterion for each electronic self-consistent cycle is no more than 1×10^{-7} eV/cell. $15 \times 15 \times 3$ Γ-centered Monkhorst–Pack k-point mesh is set in our calculations. We take the following electronic configurations: $3s^2 3p^6 3d^5 4s^2$ for Mn, $5s^2 5p^3$ for Sb and $5s^2 5p^4$ for Te. The semi-core $3s$ and $3p$ electrons of Mn are included to obtain more accurate results. The Gaussian smearing with a smearing width of 0.01 eV is adopted in our calculations. In order to appropriately describe weak interlayer interactions, we use the DFT-D3 method with Becke–Jonson damping [68, 69]. The parameters of the damping function for SCAN functional follows the work of Brandenburg *et al* [70]. We project the Bloch states to Wannier functions and build the tight-binding Hamiltonian via Wannier90 interface [71, 72]. The topological properties and AHC are calculated with the WannierTools package and the irvsp codes [73, 74]. $201 \times 201 \times 201$ k-mesh is adopted for the AHC calculation. The magnetization direction for spin–orbit coupling (SOC) electronic structure calculations is labeled along the calculated magnetic easy axis. Based on the projected tight-binding Hamiltonian, we screened the positions of the touched nodes between nearby bands in the 1 meV energy range near the Fermi level using the 'Findnodes' function of the WannierTools codes. The Weyl points must emerge pair by pair at $\pm\boldsymbol{k}$ points and they gives a pair of ± 1 chirality. Thus, we calculated the chirality of the obtained touched nodes via the WannierTools codes. If they give a pair of ± 1 chirality, we can confirm that they are Weyl nodes pairs.

3. Results and discussions

3.1. Structures and electronic properties of $MnSb_4Te_7$

The primitive cell of $MnSb_4Te_7$ is shown in figure 1(a), which is of the P-$3m1$ space group (No. 164). It consists of a $MnSb_2Te_4$ septuple layer (SL) and a Sb_2Te_3 quintuple layer (QL) stacked by van der Waals interaction along c direction, in which the $MnSb_2Te_4$ SL is stacked by 'Te–Sb–Te–Mn–Te–Sb–Te' order [38]. Here, the effect of possible intrinsic Te vacancy and Mn–Sb site mixing, which may stabilize the FM order [75–77], is considered through charge doping. The optimized lattice parameters and the corresponding experimental values are listed in table 1. It can be seen that our optimized lattice parameters are excellent in line with the experimental results. Our calculated magnetic easy axis is along c axis while the magnetic ground state is interlayer AFM state, also the same as experiments [38]. The band structure and projected density of states (PDOS) with FM and AFM configurations along the magnetic easy axis are shown in figures 1(b)–(e). It is obvious that the density of states near the Fermi level are mainly contributed by the Sb 5p and Te 5p orbitals. The calculated magnetic moment of Mn^{2+} ion is 5 μ_B, also in line with experiments [38].

3.2. The compressive strain states of $MnSb_4Te_7$

We continue to simulate the behavior of $MnSb_4Te_7$ under compressive strain along c axis. The c lattice parameter is artificially reduced while the a, b axes are optimized. Since the experimental synthesized sample is slightly hole doped by intrinsic defects, we perform our calculation for compressive strain in ideal crystal and hole doped 0.05/f.u. conditions, respectively. In both cases, $MnSb_4Te_7$ transits from an interlayer AFM ground state to a FM ground state if the c axis is reduced by no less than 6%, as shown in figures 2(a) and (b). Although the intralayer ferromagnetism is degraded in this process, it dose remain in a robust intralayer FM ground state with a relatively large energy difference more than 10 meV/f.u. between intralayer AFM states and the FM ground state throughout our simulations. To explore the underlying magnetic exchange mechanism, we have carefully checked the variance of the Mn–Te–Mn bond angle when strain is applied. We find that the Mn–Te–Mn bond angle enlarged from about 93° to 98° as shown in figure 2(a), which is a typical feature of super exchange interaction according to the Goodenough–Kanamori rule, analogous to the case of $MnBi_2Te_4$, CrI_3 and $Cr_2Ge_2Te_6$ [21, 78, 79]. As for the interlayer case, Huan *et al* [38] expected that there exists long range RKKY exchange from their experimental results. Here, we note that as c lattice parameter is reduced, the energy of the interlayer AFM state is lowered relatively to the FM state in the initial stage of compressive strain less than 4%. As the compressive strain increases, the FM state becomes more and more energetically favorable. As shown in figure 2(b), this evolution is more obvious in the 0.05 hole/f.u. charge doped case than the ideal structure. We suggest that this is also the character of RKKY exchange since such magnetic exchange is typically mediated by conduction electrons [59]. We also calculate the deformation charge density of $MnSb_4Te_7$ between no charge doped and hole doped states. As shown in figures 3(a) and (b), the carriers extensively exist in the whole unit cell. Based on the above analysis, it is expected that the magnetic exchange is dominated by the intralayer super exchange and interlayer RKKY like long range magnetic exchange. Furthermore, the magnetic easy axis can be reorientated from out-of-plane to in-plane when c parameter is

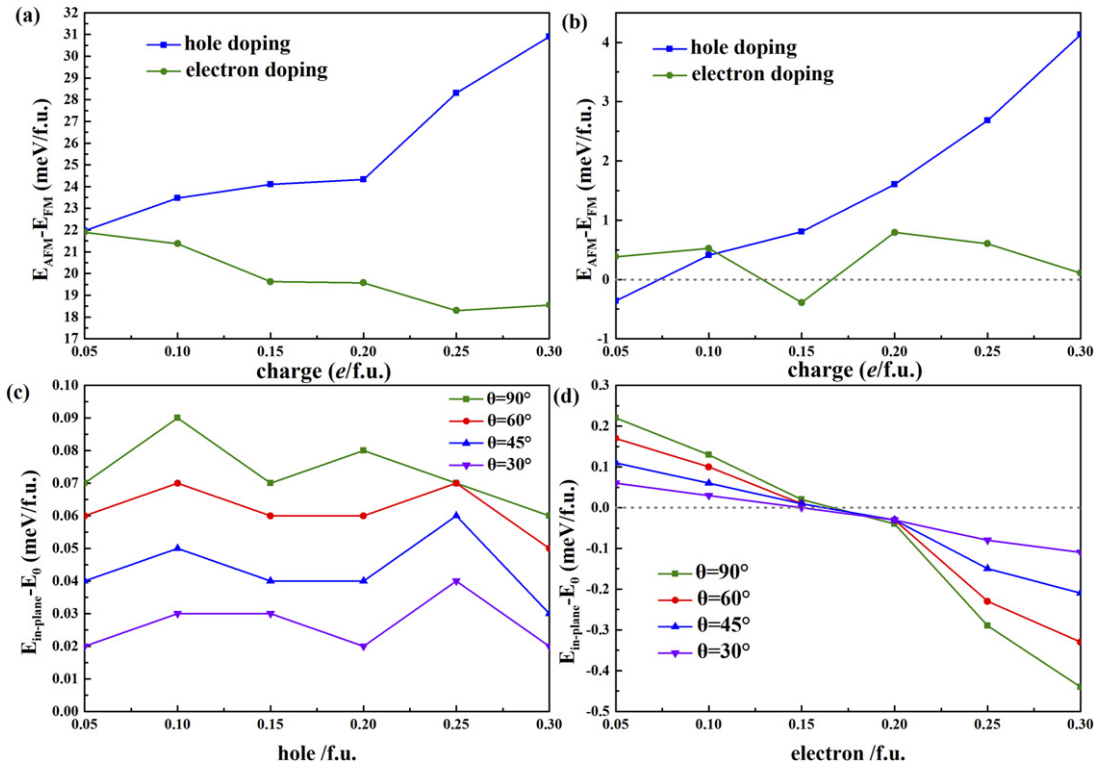

Figure 5. The AFM–FM transition and magnetic easy axis reorientation of $MnSb_4Te_7$ under charge doping. (a) The variance of intralayer magnetic exchange energy as charge doping, (b) the variance of interlayer magnetic exchange energy as charge doping, (c) the variance of MAE as hole doping, (d) the variance of MAE as electron doping.

compressed more than 10%, which will lower the symmetry of the system. Such phenomenon also emerged in $MnBi_2Te_4$ [54]. We carefully confirm that the magnetic easy axis is abruptly reoriented at the critical point rather than rotates continuously by calculating the relative energy at different magnetization directions, as shown in figures 2(c) and (d).

Although the ideal $MnSb_4Te_7$ crystal is an axion insulator in FM state, we predict that it could transit into a metallic state if *c* lattice parameter compressed more than 8%, as shown in figures 4(a) and (b). We also find that there are multiple Weyl nodes in both conduction and valence bands nearby the Fermi level as Huan *et al* [38] reported. Meanwhile, these Weyl nodes can still exist when compressive strain is applied, as listed in table 2. The calculated AHC is shown in figure 4(c). Hence, $MnSb_4Te_7$ could finally be manipulated to the FM semimetal ground state with multiple Weyl points in such *c*-compression process. We believe that such relatively large compressive strain is possible to achieve in experiments since the $MnSb_2Te_4$ SLs coupled with the Sb_2Te_3 QLs via weak van der Waals interaction and the extreme tensile strain states has been successfully realized in even more complex oxide membrances in recent years [80].

3.3. The charge doped states of $MnSb_4Te_7$

We have further explored the charge doped states of $MnSb_4Te_7$ for both electron doped and hole doped cases. In our simulations, the FM state of $MnSb_4Te_7$ is stabilized as the hole doping concentration increases and the AFM–FM transition occurs before the doping concentration reaches 0.1 hole/f.u., as shown in figures 5(a) and (b). The magnetic easy axis does not reorientate but remains in *c* direction through all the simulations under hole doping. Meanwhile, the MAE stays in a range of about 0.06 to 0.09 meV/f.u. in this process, as shown in figure 5(c). As shown in figure 6(a), we also note that the band structure does not change very much as we increase the hole concentration, suggesting that the electronic structure may not vary sharply but only the carrier concentration increases. Furthermore, there are multiple Weyl nodes near the Fermi level in hole doping concentrations of 0.05 and 0.1 hole/f.u., as listed in table 1. The induced AHC is shown in figure 6(e). As for higher hole concentrations, although there still considerable Weyl nodes exist in the valence bands, their positions are a little far away from the Fermi energy so they are not included in our consideration. Thus, we predict that $MnSb_4Te_7$ may enter a FM semimetal ground state with multiple Weyl nodes when hole doping is applied. It is worth to note that the σ_{xy} component of AHC is significantly larger than the other two components. This is ascribed to the dominated magnetization of 5 μ_B/Mn in *z* direction, in line with the earlier discussion of AHC [81].

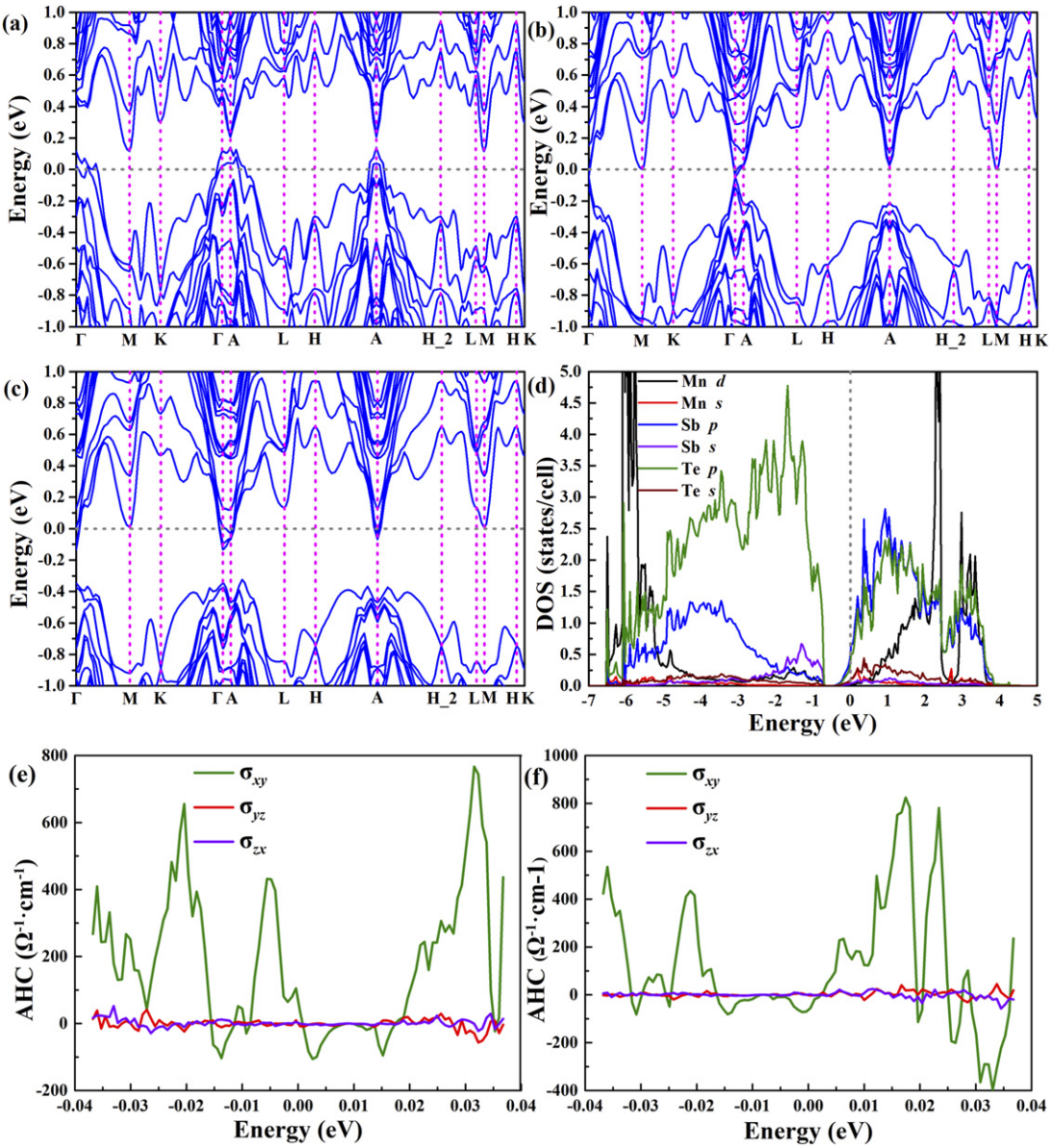

Figure 6. The electronic structure of $MnSb_4Te_7$ under charge doping. The band structure when charge doped (a) 0.3 hole/f.u., (b) 0.1 electron/f.u., (c) 0.3 electron/f.u., and (d) the PDOS when charge doped 0.3 electron/f.u., (e) the AHC when charge doped 0.05 hole/f.u., (f) the AHC when charge doped 0.05 electron/f.u.

In the electron doping case, things are quite different from the situation of the hole doping in our calculation. As the electron doping concentration increases, the energy difference of the AFM and FM states oscillates, but $MnSb_4Te_7$ may be in the interlayer AFM ground state only at the 0.15 electron/f.u. in our simulations, as shown in figures 5(a) and (b). Moreover, the magnetic easy axis is reorientated to the in-plane direction like the *c*-compression case, as shown in figure 5(d). It is worth to note that at Γ point the band gap between the conduction and valence bands is closed at 0.1, 0.15 electron/f.u. doping concentration and reopened again at higher electron doping concentrations, as shown in figures 6(b) and (c). Amazingly, the MAE could reach a very large value of 0.25, 0.44 meV/f.u. when the electron doping concentration reaches 0.25, 0.3 electron/f.u., respectively. We suggest that the enhancement of MAE may originate from the occupancy of the 5*p* orbitals of Sb, Te, as shown in figure 6(d). Such large value of MAE is several orders greater than the typical room-temperature magnetic element crystals, such as Fe, Co and Ni, of which the MAE values are generally on the order of 1 μeV [82]. Generally speaking, materials with such large MAE meet the requirement for spintronics applications. Last but not the least, we further find Weyl points in the conduction bands near the Fermi level at the electron doping concentration of 0.05 electron/f.u., as listed in table 2. Notable AHC is predicted as shown in figure 6(f). Therefore, electron doped $MnSb_4Te_7$ can also behave as an FM semimetal with multiple Weyl nodes like the hole doped case.

4. Summary

To draw conclusions, we have systematically studied the magnetic and topological properties of $MnSb_4Te_7$ under compressive strain and charge doping conditions using first-principles calculations. Via SCAN + U method, AFM–FM transition is expected in $MnSb_4Te_7$ under strain or hole doping. Multiple Weyl nodes are found in both conduction and valence bands, and therefore $MnSb_4Te_7$ may behave as a semimetal with multiple Weyl points in these FM ground states. Notable AHC of σ_{xy} is also predicted in our calculations due to the dominated out of plane magnetization. At the same time, the magnetic easy axis is reorientated from out-of-plane to in-plane direction when the c-compression strain or electron doping concentration reaches the critical point, changing the symmetry of the system. Meanwhile, the MAE can reach a large value of 0.44 meV/f.u. when $MnSb_4Te_7$ is electron doped 0.3 electron/f.u. Based on our calculation results, we further expect that the underlying magnetic exchange mechanisms are intralayer Mn–Te–Mn super exchange and interlayer RKKY like exchange. Thus, a feasible way to tune the magnetic-topological properties and a comprehensive theoretical understanding of this multiple magnetic van der Waals material is provided in this work.

Acknowledgments

This work is financially supported by NSFC (Grant No. 12074126), the Foundation for Innovative Research Groups of the National Natural Science Foundation of China (Grant No. 51621001), the Fundamental Research Funds for the Central Universities (Grant No. 2020ZYGXZR076), the Guangdong Basic and Applied Basic Research Foundation (No. 2021A1515010349) and the Guangzhou Basic and Applied Basic Research Foundation (No. 202102080166).

Data availability statement

The data that support the findings of this study are available upon reasonable request from the authors.

ORCID iDs

Xiao-Bao Yang https://orcid.org/0000-0001-8851-1988
Yu-Jun Zhao https://orcid.org/0000-0002-6923-1099

References

[1] Moore J E 2010 *Nature* **464** 194–8
[2] Haldane F D M 1988 *Phys. Rev. Lett.* **61** 2015–8
[3] Kane C L and Mele E J 2005 *Phys. Rev. Lett.* **95** 226801
[4] Fu L and Kane C L 2006 *Phys. Rev.* B **74** 195312
[5] Yu R, Zhang W, Zhang H J, Zhang S C, Dai X and Fang Z 2010 *Science* **329** 61–4
[6] Onoda M and Nagaosa N 2003 *Phys. Rev. Lett.* **90** 206601
[7] Zhang H, Liu C X, Qi X L, Dai X, Fang Z and Zhang S C 2009 *Nat. Phys.* **5** 438–42
[8] Liu C C, Feng W and Yao Y 2011 *Phys. Rev. Lett.* **107** 076802
[9] Pesin D and Balents L 2010 *Nat. Phys.* **6** 376–81
[10] Kim K *et al* 2018 *Nat. Mater.* **17** 794–9
[11] Yang Y, Lu J, Yan M, Huang X, Deng W and Liu Z 2021 *Phys. Rev. Lett.* **126** 156801
[12] Chen Z J, Wang R, Xia B W, Zheng B B, Jin Y J, Zhao Y J and Xu H 2021 *Phys. Rev. Lett.* **126** 185301
[13] Tang F, Po H C, Vishwanath A and Wan X 2019 *Nature* **566** 486–9
[14] Vergniory M G, Elcoro L, Felser C, Regnault N, Bernevig B A and Wang Z 2019 *Nature* **566** 480–5
[15] Weng H, Fang C, Fang Z, Bernevig B A and Dai X 2015 *Phys. Rev.* X **5** 011029
[16] Lv B Q *et al* 2015 *Nat. Phys.* **11** 724–7
[17] Chang C-Z *et al* 2013 *Science* **340** 167–70
[18] Qi X L, Hughes T L and Zhang S C 2008 *Phys. Rev.* B **78** 195424
[19] Lv B Q *et al* 2017 *Nature* **546** 627–31
[20] Otrokov M M *et al* 2019 *Nature* **576** 416–22
[21] Li J, Li Y, Du S, Wang Z, Gu B L, Zhang S C, He K, Duan W and Xu Y 2019 *Sci. Adv.* **5** eaaw5685
[22] Zhang D, Shi M, Zhu T, Xing D, Zhang H and Wang J 2019 *Phys. Rev. Lett.* **122** 206401
[23] Wan X, Turner A M, Vishwanath A and Savrasov S Y 2011 *Phys. Rev.* B **83** 205101
[24] Deng Y, Yu Y, Shi M Z, Guo Z, Xu Z, Wang J, Chen X H and Zhang Y 2020 *Science* **367** 895–900
[25] Lei C and MacDonald A H 2021 *Phys. Rev. Mater.* **5** L051201
[26] Rienks E D L *et al* 2019 *Nature* **576** 423–8
[27] Hu C *et al* 2020 *Sci. Adv.* **6** eaba4275

[28] Deng H et al 2021 Nat. Phys. 17 36–42
[29] Hu C et al 2020 Nat. Commun. 11 97
[30] Wang L et al 2021 Nat. Commun. 12 2361
[31] Zhang X and Liu F 2021 Phys. Rev. B 103 024405
[32] Liu C et al 2020 Nat. Mater. 19 522–7
[33] Zhang D, Shi M, Zhu T, Xing D, Zhang H and Wang J 2019 Phys. Rev. Lett. 122 206401
[34] Garrity K F, Chowdhury S and Tavazza F M 2021 Phys. Rev. Mater. 5 024207
[35] Chen Y J et al 2019 Phys. Rev. X 9 041040
[36] Zhou L, Tan Z, Yan D, Fang Z, Shi Y and Weng H 2020 Phys. Rev. B 102 085114
[37] Eremeev S V, Rusinov I P, Koroteev Y M, Vyazovskaya A Y, Hoffmann M, Echenique P M, Ernst A, Otrokov M M and Chulkov E V 2021 J. Phys. Chem. Lett. 12 4268–77
[38] Huan S et al 2021 Phys. Rev. Lett. 126 246601
[39] Zheng G et al 2020 Phys. Rev. Lett. 125 047202
[40] Xie W Q, Lu Z W, He C C, Yang X B and Zhao Y J 2021 J. Phys.: Condens. Matter. 33 215803
[41] Chen B et al 2019 Nat. Commun. 10 4469
[42] Chen K Y, Wang B S, Yan J Q, Parker D S, Zhou J S, Uwatoko Y and Cheng J G 2019 Phys. Rev. Mater. 3 094201
[43] Huang Z, Du M H, Yan J and Wu W 2020 Phys. Rev. Mater. 4 121202(R)
[44] Lai Y, Ke L, Yan J, McDonald R D and McQueeney R J 2021 Phys. Rev. B 103 184429
[45] Lapano J et al 2020 Phys. Rev. Mater. 4 111201(R)
[46] Lei C, Heinonen O, MacDonald A H and McQueeney R J 2021 Phys. Rev. Mater. 5 064201
[47] Lian B, Liu Z, Zhang Y and Wang J 2020 Phys. Rev. Lett. 124 126402
[48] Murakami T, Nambu Y, Koretsune T, Xiangyu G, Yamamoto T, Brown C M and Kageyama H 2019 Phys. Rev. B 100 195103
[49] Nevola D, Li H X, Yan J Q, Moore R G, Lee H N, Miao H and Johnson P D 2020 Phys. Rev. Lett. 125 117205
[50] Otrokov M M et al 2019 Phys. Rev. Lett. 122 107202
[51] Shao J et al 2021 Nano Lett. 21 5874–80
[52] Tan A, Labracherie V, Kunchur N, Wolter A U B, Cornejo J, Dufouleur J, Büchner B, Isaeva A and Giraud R 2020 Phys. Rev. Lett. 124 197201
[53] Wei P and Moodera J S 2020 Nat. Mater. 19 481–2
[54] Xue F, Wang Z, Hou Y, Gu L and Wu R 2020 Phys. Rev. B 101 184426
[55] Yan J Q, Liu Y H, Parker D S, Wu Y, Aczel A A, Matsuda M, McGuire M A and Sales B C 2020 Phys. Rev. Mater. 4 054202
[56] Yang S et al 2021 Phys. Rev. X 11 011003
[57] Zhang H, Yang W, Wang Y and Xu X 2021 Phys. Rev. B 103 094433
[58] Lee S H et al 2021 Phys. Rev. X 11 031032
[59] Zhao Y J, Shishidou T and Freeman A J 2003 Phys. Rev. Lett. 90 047204
[60] Liechtenstein A I, Anisimov V I and Zaanen J 1995 Phys. Rev. B 52 R5467–70
[61] Kresse G and Furthmüller J 1996 Phys. Rev. B 54 11169–86
[62] Kresse G and Furthmüller J 1996 Comput. Mater. Sci. 6 15–50
[63] Kresse G and Hafner J 1993 Phys. Rev. B 48 13115–8
[64] Kresse G and Hafner J 1993 Phys. Rev. B 47 558–61
[65] Kresse G and Joubert D 1999 Phys. Rev. B 59 1758–75
[66] Sun J, Ruzsinszky A and Perdew J P 2015 Phys. Rev. Lett. 115 036402
[67] Sun J et al 2016 Nat. Chem. 8 831–6
[68] Grimme S, Antony J, Ehrlich S and Krieg H 2010 J. Chem. Phys. 132 154104
[69] Grimme S, Ehrlich S and Goerigk L 2011 J. Comput. Chem. 32 1456–65
[70] Brandenburg J G, Bates J E, Sun J and Perdew J P 2016 Phys. Rev. B 94 115144
[71] Mostofi A A, Yates J R, Lee Y S, Souza I, Vanderbilt D and Marzari N 2008 Comput. Phys. Commun. 178 685–99
[72] Marzari N, Mostofi A A, Yates J R, Souza I and Vanderbilt D 2012 Rev. Mod. Phys. 84 1419–75
[73] Wu Q, Zhang S, Song H F, Troyer M and Soluyanov A A 2018 Comput. Phys. Commun. 224 405–16
[74] Gao J, Wu Q, Persson C and Wang Z 2021 Comput. Phys. Commun. 261 107760
[75] Liu Y et al 2021 Phys. Rev. X 11 021033
[76] Hou F et al 2020 ACS Nano 14 11262–72
[77] Du M H, Yan J, Cooper V R and Eisenbach M 2021 Adv. Funct. Mater. 31 2006516
[78] Huang B et al 2017 Nature 546 270–3
[79] Gong C et al 2017 Nature 546 265–9
[80] Hong S S et al 2020 Science 368 71–6
[81] Yao Y, Kleinman L, MacDonald A H, Sinova J, Jungwirth T, Wang D S, Wang E and Niu Q 2004 Phys. Rev. Lett. 92 037204
[82] Halilov S V, Perlov A Y, Oppeneer P M, Yaresko A N and Antonov V N 1998 Phys. Rev. B 57 9557–60